

Article

Isostructural Oxides $\text{Sr}_3\text{Ti}_{2-x}\text{M}_x\text{O}_{7-\delta}$ ($\text{M} = \text{Mn, Fe, Co}$; $x = 0, 1$) as Electrocatalysts for Water Splitting

Chandana C. W. Kananke-Gamage and Farshid Ramezanipour *

Department of Chemistry, University of Louisville, Louisville, KY 40292, USA

* Correspondence: farshid.ramezanipour@louisville.edu; Tel.: +1-(502)-852-7061

Abstract: The correlation of the electrocatalytic activity with electrical conductivity, oxygen-vacancies, and electronegativity have been studied in a series of isostructural oxides, having the so-called Ruddlesden-Popper structure. The structures of these materials comprise transition metals that are octahedrally coordinated to form a network of bilayer stacks. These materials are catalytically active for both half-reactions of water-splitting, namely oxygen-evolution reaction (OER) and hydrogen-evolution reaction (HER). They show a systematic increase in electrocatalytic activity in progression from $\text{Sr}_3\text{Ti}_2\text{O}_7$ to $\text{Sr}_3\text{TiMnO}_7$, $\text{Sr}_3\text{TiFeO}_{7-\delta}$, and $\text{Sr}_3\text{TiCoO}_{7-\delta}$. The kinetic studies using the Tafel method indicate the same trend across the series, where the best catalyst also has the fastest kinetics for both HER and OER. In addition, the same progression is observed in the concentration of oxygen-vacancies, as well as the electrical conductivity in a wide range of temperatures, 25 °C–800 °C. The material that shows the best electrocatalytic activity, i.e., $\text{Sr}_3\text{TiCoO}_{7-\delta}$, also has the highest electrical conductivity and the greatest concentration of oxygen vacancies in the series. The correlations observed in this work indicate that trends in electrocatalytic performance may be related to the systematic increase in electrical conductivity, electronegativity, and oxygen-vacancies, as well as the electron occupancy of e_g orbitals, which can affect the strength of sigma interactions between the catalyst and reaction intermediates.



Citation: Kananke-Gamage, C.C.W.; Ramezanipour, F. Isostructural Oxides $\text{Sr}_3\text{Ti}_{2-x}\text{M}_x\text{O}_{7-\delta}$ ($\text{M} = \text{Mn, Fe, Co}$; $x = 0, 1$) as Electrocatalysts for Water Splitting. *Inorganics* **2023**, *11*, 172. <https://doi.org/10.3390/inorganics11040172>

Academic Editors: Richard Dronskowski, Christian Julien, Rainer Niewa, Alexander Novikov, Gary Hix and Hans-Conrad zur Loye

Received: 1 March 2023

Revised: 14 April 2023

Accepted: 16 April 2023

Published: 19 April 2023



Copyright: © 2023 by the authors. Licensee MDPI, Basel, Switzerland. This article is an open access article distributed under the terms and conditions of the Creative Commons Attribution (CC BY) license (<https://creativecommons.org/licenses/by/4.0/>).

Keywords: oxygen-evolution reaction; hydrogen-evolution reaction; water splitting; solid-state structures; electrocatalysis

1. Introduction

Perovskite-based oxides show a variety of interesting properties, such as electrical conductivity, magnetism, and electrocatalytic activity [1–4]. The quasi-two-dimensional Ruddlesden Popper (RP) structure with formula $\text{A}_{n-1}\text{A}'_2\text{B}_n\text{O}_{3n+1}$ (Figure 1) is derived from perovskite, and consists of stacks of corner-sharing BO_6 octahedra, where B is often a transition metal. The number of octahedral layers in each stack is represented in the formula by n . The spaces between stacks are often occupied by lanthanide or alkaline-earth metals (A' -site metals), which also reside in intra-stack spaces (A-site) between the octahedra. Some applications of RP materials, such as energy storage, electrocatalysis, and oxide/lithium-ion conductivity, have been studied, highlighting the significance of this class of materials [5–7]. The A/A' and B site modifications of RP oxides affect the structural, physical, and chemical properties. Oxygen vacancies in these oxide materials also have an impact on properties such as conductivity and electrocatalytic activity. It has been demonstrated in various studies that the conductivity and electrocatalytic properties are related to oxygen vacancies, structural changes, and compositional modifications [7–12]. The distinct properties of RP oxides are a result of a structural arrangement consisting of wide inter-stack spaces between corner-sharing BO_6 octahedra [2], with possible oxygen vacancies or interstitials.

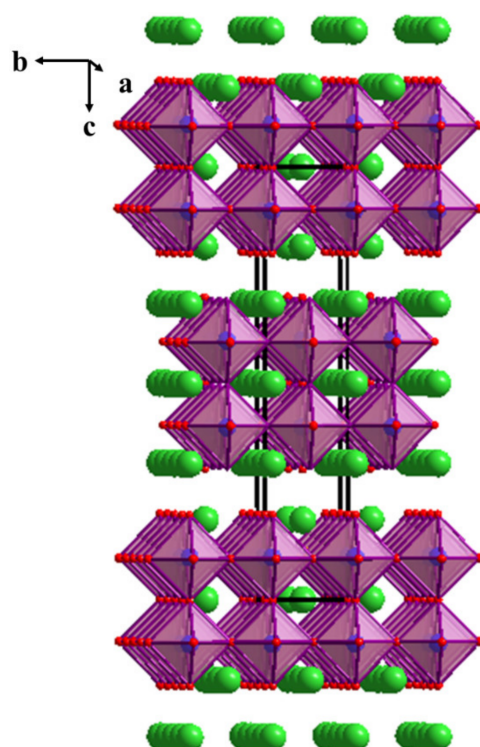


Figure 1. Crystal structure of Sr_3TiMO_7 ($M = \text{Ti, Mn, Fe, Co}$). Green spheres represent La, and red spheres show oxygens. The BO_6 octahedra are shown purple in color.

One area where RP oxides can be utilized is water electrolysis. Two fundamental reactions in electrochemical water splitting are the generation of hydrogen and oxygen gases in the two electrodes. The sluggish kinetics of these reactions require the utilization of catalysts that can facilitate these processes. Discovering active catalysts that can help these reactions occur at lower potentials is therefore essential [10,13]. The RP oxides have shown great promise as efficient catalysts for water-splitting, drawing interest in the further investigation of the activities of these oxides [7,13]. Various methods have been used to enhance the catalytic activities of these materials. For example, the electrocatalytic activity of the single-layered RP oxide, $\text{La}_{0.5}\text{Sr}_{1.5}\text{Ni}_{1-x}\text{Fe}_x\text{O}_{4\pm\delta}$ has been studied by changing the degree of Fe substitution at the B-site, where all materials in the series crystallize in the tetragonal $I4/mmm$ space group. The two parent compounds, $\text{La}_{0.5}\text{Sr}_{1.5}\text{NiO}_4$ and $\text{La}_{0.5}\text{Sr}_{1.5}\text{FeO}_4$, show OER overpotentials of ~ 500 mV and ~ 550 mV in 0.1 M KOH, respectively, as compared to ~ 460 mV for $\text{La}_{0.5}\text{Sr}_{1.5}\text{Ni}_{1-x}\text{Fe}_x\text{O}_{4\pm\delta}$ ($x = 0.85$) [14]. Another example is the B-site substitution to study the improvement of the catalytic performance of $\text{La}_{1.5}\text{Sr}_{0.5}\text{NiO}_4$. The catalytic activity of $\text{La}_{1.5}\text{Sr}_{0.5}\text{Ni}_{0.5}\text{Co}_{0.5}\text{O}_4$, with an OER overpotential of ~ 470 mV, is better than that of the parent compound, $\text{La}_{1.5}\text{Sr}_{0.5}\text{NiO}_4$, which shows an overpotential of ~ 510 mV in 0.1 M KOH [15]. Another example is $\text{Sr}_2\text{LaCoMnO}_7$, which shows better electrocatalytic performance for both half reactions of water splitting, OER and HER, compared to $\text{Sr}_2\text{LaFeMnO}_7$ [7].

In this study, we investigate the electrocatalytic activities of a series of bilayer RP materials, $\text{A}_{n-1}\text{A}'_2\text{B}_n\text{O}_{3n+1}$ ($n = 2$), for water electrolysis. Some other properties of these materials have been previously studied. For example, the structure, thermoelectric, and dielectric properties of $\text{Sr}_3\text{Ti}_2\text{O}_7$ (ICDD # 11-663) have been investigated [16,17]. Mixed conductivity and oxygen permeability have been studied for $\text{Sr}_3\text{Ti}_{1-x}\text{Co}_x\text{O}_7$ and $\text{Sr}_3\text{Ti}_{1-x}\text{Fe}_x\text{O}_7$ [18–20]. Low temperature electrical conductivity, magnetic properties, and dielectric response have been investigated for $\text{Sr}_3\text{TiMnO}_7$ [21–23]. In this work, we focus on a different property, namely electrocatalytic activity, and demonstrate systematic trends in the series $\text{Sr}_3\text{Ti}_{2-x}\text{M}_x\text{O}_{7-\delta}$ ($M = \text{Mn, Fe, Co}$; $x = 0, 1$). We also show the creation of oxygen vacancies and their correlations with electrocatalytic and charge-transport properties.

2. Results and Discussion

2.1. Crystal Structure and Oxygen Content

The crystal structures of the materials were verified by Rietveld refinements using powder X-ray diffraction data. The refinement profiles are shown in Figure 2 and the refined structural parameters are listed in Tables 1–4. The quasi-two-dimensional network of these RP materials, $A_{n-1}A'_2B_nO_{3n+1}$ ($n = 2$), consists of bilayer stacks of BO_6 octahedra, where the B-site is occupied by transition metals. The spaces between the octahedra are occupied by A and A' metals, which reside on intra-stack and inter-stack sites, with coordination numbers 12 and 9, respectively. In the materials studied here, both A and A' sites are occupied by Sr. On the other hand, the B-site is occupied by Ti in $Sr_3Ti_2O_7$ [24]; and a mix of Ti/Mn, Ti/Fe, or Ti/Co for Sr_3TiMnO_7 [22], $Sr_3TiFeO_{7-\delta}$, [25], and $Sr_3TiCoO_{7-\delta}$ [19], respectively.

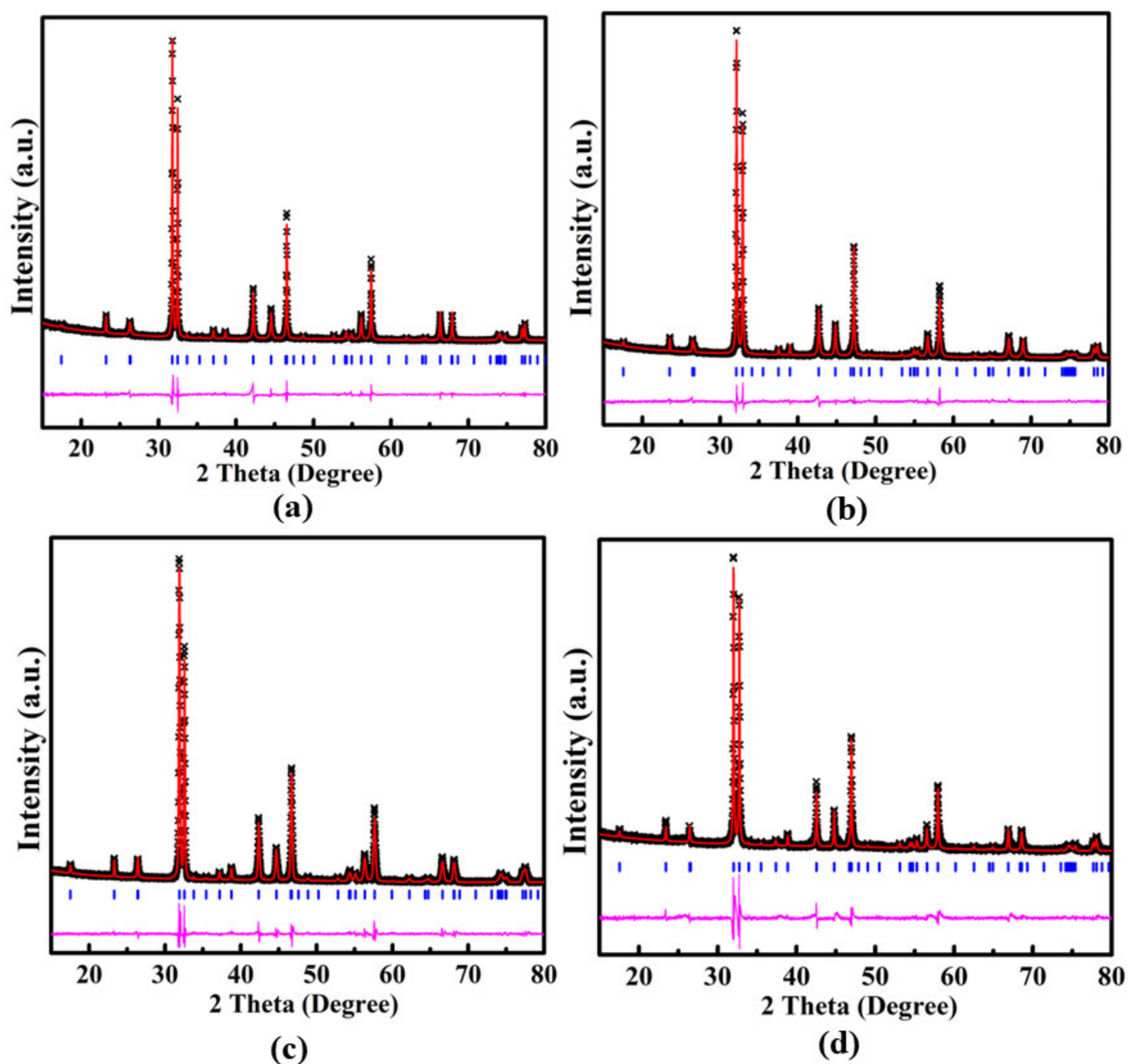


Figure 2. Rietveld refinement profiles with powder X-ray diffraction data for (a) $Sr_3Ti_2O_7$, (b) Sr_3TiMnO_7 , (c) $Sr_3TiFeO_{7-\delta}$, and (d) $Sr_3TiCoO_{7-\delta}$. The experimental data are represented by black crosses. The red line shows the fit. The vertical blue tick marks and the lower pink line correspond to the Bragg peak positions and difference plot, respectively.

Table 1. Refined structural parameters of Sr₃Ti₂O₇ from powder X-ray diffraction data. Space group: I4/mmm, $a = b = 3.9009(1)$ Å, $c = 20.3386(5)$ Å, Rp = 0.0702, wRp = 0.0949.

Atom	x	y	z	Occupancy	U _{iso} (Å ²)	Multiplicity
Sr1	0	0	0.5	1	0.0327(18)	2
Sr2	0	0	0.31421(16)	1	0.0390(18)	4
Ti	0	0	0.09932(27)	1	0.0158(28)	4
O1	0	0	0	1	0.090(8)	2
O2	0	0	0.1882(12)	1	0.090(8)	4
O3	0	0.5	0.0979(6)	1	0.090(8)	8

Table 2. Refined structural parameters of Sr₃TiMnO₇ from powder X-ray diffraction data. Space group: I4/mmm, $a = b = 3.8481(1)$ Å, $c = 20.2024(6)$ Å, Rp = 0.0446, wRp = 0.0585.

Atom	x	y	z	Occupancy	U _{iso} (Å ²)	Multiplicity
Sr1	0	0	0.5	1	0.021(4)	2
Sr2	0	0	0.30097(12)	1	0.040(4)	4
Ti	0	0	0.11764(17)	0.5	0.034(4)	4
Mn	0	0	0.11764(17)	0.5	0.034(4)	4
O1	0	0	0	1	0.039(5)	2
O2	0	0	0.1897(7)	1	0.039(5)	4
O3	0	0.5	0.0759(4)	1	0.039(5)	8

Table 3. Refined structural parameters of Sr₃TiFeO_{7-δ} from powder X-ray diffraction data. Space group: I4/mmm, $a = b = 3.8904(1)$ Å, $c = 20.2788(7)$ Å, Rp = 0.0326, wRp = 0.0459.

Atom	x	y	z	Occupancy	U _{iso} (Å ²)	Multiplicity
Sr1	0	0	0.5	1	0.0083(13)	2
Sr2	0	0	0.31585(9)	1	0.0148(10)	4
Ti	0	0	0.10014(20)	0.5	0.0010(9)	4
Fe	0	0	0.10014(20)	0.5	0.0010(9)	4
O1	0	0	0	1	0.0542(17)	2
O2	0	0	0.1980(6)	1	0.0542(17)	4
O3	0	0.5	0.0963(4)	1	0.0542(17)	8

Table 4. Refined structural parameters of Sr₃TiCoO_{7-δ} from powder X-ray diffraction data. Space group: I4/mmm, $a = b = 3.8682(1)$ Å, $c = 20.2349(8)$ Å, Rp = 0.0361, wRp = 0.0545.

Atom	x	y	z	Occupancy	U _{iso} (Å ²)	Multiplicity
Sr1	0	0	0	1	0.031(6)	2
Sr2	0	0	0.18493(21)	1	0.052(6)	4
Ti	0	0	0.4010(5)	0.5	0.050(6)	4
Co	0	0	0.4010(5)	0.5	0.050(6)	4
O1	0	0	0.5	1	0.080(8)	2
O2	0	0	0.3126(13)	1	0.080(8)	4
O3	0	0.5	0.0940(11)	1	0.080(8)	8

Iodometric titrations were carried out to examine the oxygen stoichiometries, which indicated 7 oxygens per formula unit for $\text{Sr}_3\text{Ti}_2\text{O}_7$ and $\text{Sr}_3\text{TiMnO}_7$, but 6.76 and 6.62 oxygens per formula unit for $\text{Sr}_3\text{TiFeO}_{7-\delta}$ and $\text{Sr}_3\text{TiCoO}_{7-\delta}$, respectively. We note that all materials were synthesized under similar conditions in air, and no reduction experiment was conducted on any of these materials. It appears that the latter two materials have a tendency to accommodate cations with a lower oxidation state, possibly due to the relative stability of trivalent iron and cobalt. These findings are consistent with the observation of larger unit cell volumes for $\text{Sr}_3\text{TiFeO}_{7-\delta}$ [25] and $\text{Sr}_3\text{TiCoO}_{7-\delta}$, [19], indicating more reduced transition metals due to the lower oxygen stoichiometry. We note that ionic radii [26] of Fe^{3+} (0.645 Å) and Co^{3+} (0.61 Å) are considerably larger than those of Fe^{4+} (0.585 Å) and Co^{4+} (0.53 Å), respectively.

As shown in Table 5, the BO_6 octahedra in these materials are distorted, where the axial bond lengths are dissimilar. The distortions are also evident from the B-O-B bond angles, which deviate from the ideal 180° . $\text{Sr}_3\text{TiMnO}_7$ exhibits the highest distortion of angles, while $\text{Sr}_3\text{Ti}_2\text{O}_7$ exhibits the lowest, as indicated by the bond angles reported in Table 5.

Table 5. B-O bond distances and B-O-B angles for the synthesized structures.

$\text{Sr}_3\text{Ti}_2\text{O}_7$		$\text{Sr}_3\text{TiMnO}_7$	
Ti-O1	2.020(6)	Ti/Mn-O1	2.3766(35)
Ti-O2	1.808(23)	Ti/Mn-O2	1.456(12)
Ti-O3 × 4	1.95065(20)	Ti/Mn-O3 × 4	2.1006(31)
Average Ti-O	1.9384(19)	Average Ti/Mn-O	2.0391(29)
Ti-O1-Ti	180.0(0)	Ti/Mn-O1-Ti/Mn	180.0(0)
Ti-O3-Ti	178.3 (8)	Ti/Mn-O3-Ti/Mn	132.7(4)
Average Ti-O-Ti	179.2(6)	Average Ti/Mn-O-Ti/Mn	156.35(3)
$\text{Sr}_3\text{TiFeO}_{7-\delta}$		$\text{Sr}_3\text{TiCoO}_{7-\delta}$	
Ti/Fe-O1	2.031(4)	Ti/Co-O1	2.003(11)
Ti/Fe-O2	1.984(13)	Ti/Co-O2	1.788(25)
Ti/Fe-O3 × 4	1.9468(4)	Ti/Co-O3 × 4	1.9367(13)
Average Ti/Fe-O	1.9670(6)	Average Ti/Co-O	1.9229(15)
Ti/Fe-O1-Ti/Fe	180.0(0)	Ti/Co-O1-Ti/Co	180.0(0)
Ti/Fe-O3-Ti/Fe	175.4(6)	Ti/Co-O3-Ti/Co	174.0(15)
Average Ti/Fe-O-Ti/Fe	177.7(4)	Average Ti/Co-O-Ti/Co	177.0(11)

Moreover, scanning electron microscopy data (Figure S1) show that $\text{Sr}_3\text{TiCoO}_{7-\delta}$ has larger grains than the other three materials.

2.2. Electrical Conductivity

The variable-temperature electrical conductivity of the synthesized materials was studied from the measured resistance (R) using the following equation at a constant applied potential:

$$\sigma = L/RA \quad (1)$$

In the above equation, σ is the conductivity, L is the average thickness, and A ($A = \pi r^2$) is the average cross-sectional area of the pellet. The conductivity values obtained for the materials from 25°C to 800°C are given in Figure 3a. The insets in Figure 3a show a magnified view of the conductivity variations for $\text{Sr}_3\text{Ti}_2\text{O}_7$ and $\text{Sr}_3\text{TiMnO}_7$. The conductivity of all materials increases as a function of temperature, a behavior typical of semiconducting materials. For $\text{Sr}_3\text{TiCoO}_{7-\delta}$ and $\text{Sr}_3\text{TiFeO}_{7-\delta}$, this increase is observed from 25°C to 500°C , followed by a decrease in conductivity as the temperature is raised to 800°C .

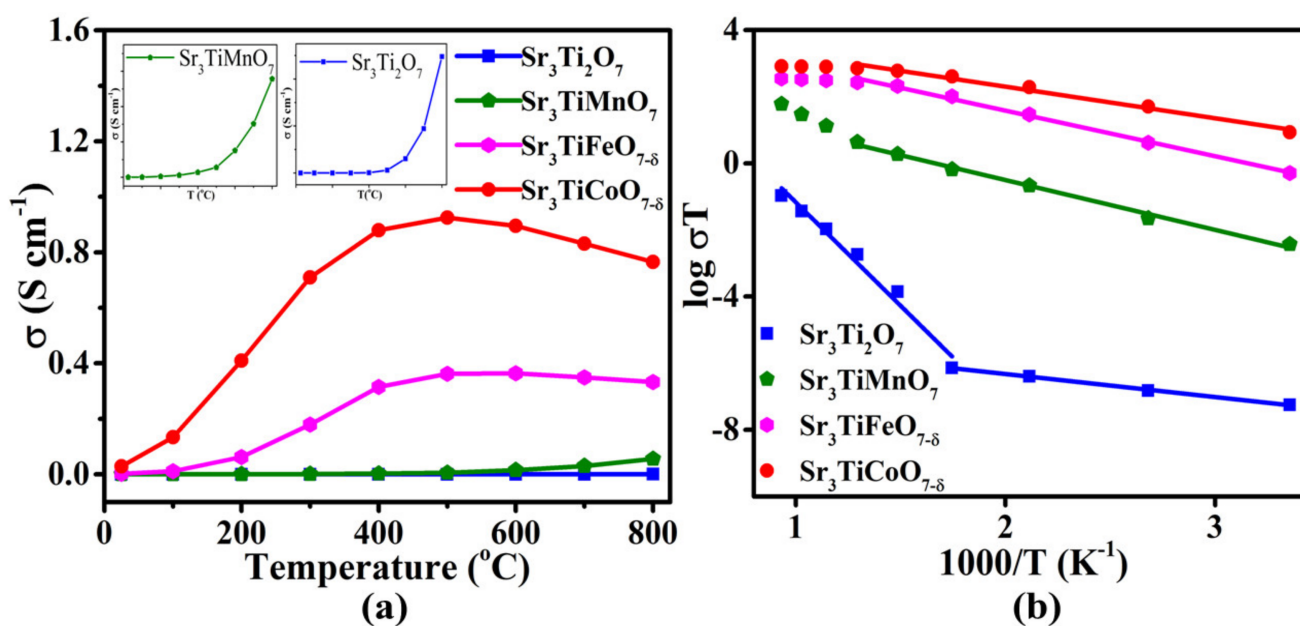


Figure 3. (a) Electrical conductivity variation as a function of temperature. The dotted box has been magnified in the inset to show the conductivity variations for Sr₃Ti₂O₇ and Sr₃TiMnO₇. (b) Arrhenius plots for determination of the activation energies (E_a) for the temperature-activated increase in conductivity.

The behavior of these materials can be described by Equation (2), where σ , n , e , and μ are conductivity, concentration of electrons/holes, charge of the electron, and mobility of the charge carriers, respectively [27]:

$$\sigma = ne\mu \quad (2)$$

The characteristic feature of a semiconductor is an increase in the number of charge carriers as a function of temperature, leading to an increased electrical conductivity. The metallic behavior, i.e., decrease in electrical conductivity as a function of temperature, is explained by an increase in collisions between phonons and charge carriers with increasing temperature, which will decrease the relaxation time; hence, lowering the charge-carrier mobility and the electrical conductivity.

The electron/hole hopping in oxides requires the B-site metal to have a variable oxidation state [8]. Considering that Mn, Fe, and Co have multiple stable oxidation states, it is expected that their presence in Sr₃TiMO₇ (M = Mn, Fe, Co) leads to a higher electrical conductivity compared to Sr₃Ti₂O₇. As shown in Table 6, Sr₃Ti₂O₇ has a room temperature conductivity that is at least five orders of magnitude lower than those of the other three materials.

Table 6. Room temperature electrical conductivities and activation energies.

Material	Conductivity at 25 °C (S/cm)	Activation Energy (eV)
Sr ₃ Ti ₂ O ₇	1.88719×10^{-10}	0.1372 (298–573 K) 1.2327 (573–1073 K)
Sr ₃ TiMnO ₇	1.2445×10^{-5}	0.2966 (298–773 K)
Sr ₃ TiFeO _{7-δ}	1.72×10^{-3}	0.2714 (298–773 K)
Sr ₃ TiCoO _{7-δ}	2.843×10^{-2}	0.1883 (298–773 K)

The electrical conduction in perovskite oxides occur through the B-O-B pathways [8], facilitated by the overlap of the transition metal 3d orbitals with oxygen 2p orbitals. Shorter B-O bonds and greater B-O-B angles facilitate the conductivity by increasing the orbital overlap [28,29]. Therefore, the degree of structural distortion in the structure has an impact on the conductivity [30]. As shown in Table 5, Sr₃TiMnO₇ exhibits the largest distortion of B-O-B angles. Distortions can hinder the overlap of B-site metal 3d orbitals with oxygen 2p orbitals, leading to lower conductivity. Greater distortions and longer B-O bonds in Sr₃TiMnO₇ may cause the material to be less conductive. As shown in Figure 3a, Sr₃TiCoO_{7-δ} shows the highest conductivity in the entire temperature range, followed by Sr₃TiFeO_{7-δ}. Oxygen vacancies were found for both materials by iodometric titrations, which indicated that Sr₃TiCoO_{7-δ} has more oxygen vacancies than Sr₃TiFeO_{7-δ}. Although B-O-B bond angles in the two materials are similar, Sr₃TiCoO_{7-δ}, has a greater conductivity than Sr₃TiFeO_{7-δ}, which may be, in part, related to its shorter average B-O bond length (Table 5), facilitating the orbital overlap [28,29].

The activation energy for the rise in thermally activated conductivity was examined using the Arrhenius equation below:

$$\sigma T = \sigma_0 e^{-\frac{E_a}{2.303 K_B T}} \quad (3)$$

In this equation, σ , σ_0 , T , E_a , and K_B represent conductivity, pre-exponential factor, temperature, activation energy, and the Boltzmann constant, respectively. Figure 3b shows the Arrhenius plots for the four materials. The calculated activation energies using slopes of the best line of fits in the Arrhenius plots are listed in Table 6. It is noted that here, the activation energy indicates the energy barrier for the temperature-dependent rise in conductivity.

2.3. Electrocatalytic Properties for HER and OER

The HER electrocatalytic activities of the synthesized materials were investigated, showing a systematic change. The overpotential, η_{10} , which is the difference between the experimentally observed potential and the thermodynamic potential at 10 mA cm⁻², is one of the important parameters used to assess the electrocatalytic activity of a catalyst. While the overpotentials of these catalysts are not as low as those of state-of-the-art HER catalysts, they show a systematic trend in their performance. As illustrated in Figure 4a, Sr₃TiCoO_{7-δ} shows the lowest overpotential, $\eta_{10} = -424$ mV, indicating better activity compared to the other materials. It is followed by Sr₃TiFeO_{7-δ}, which shows $\eta_{10} = -452$ mV. The polarization curves for Sr₃TiMnO₇ and Sr₃Ti₂O₇ do not even reach 10 mA cm⁻², indicating the low HER activities of these two compounds. The overpotential of the state-of-the-art Pt/C, [7,10] as well as those of some oxides, such as CaSrFeMnO_{6-δ} ($\eta_{10} = 390$ mV) [29] and LaCa₂Fe₃O₈ ($\eta_{10} = 400$ mV) [31], are lower than those found in this work. However, the HER overpotentials for the two best materials in this work are smaller than the values reported for some oxides such as TiO_{2-x} ($\eta_{10} = 630$ mV) [32]. The overpotentials for some other Sr-based oxides are listed in Table S1. X-ray diffraction data before and after the HER experiment (Figure 4c) show that, while some deterioration of the material might be happening, the bulk of the catalyst retains its crystalline structure. As shown in Figure 4d, chronopotentiometry measurements show a stable current response, indicating that the catalyst remains active for at least 12 h.

The kinetics of the reaction was evaluated using the Tafel equation $\eta = a + b \log j$, where η is the overpotential and j is the current density. Further information about the Tafel equation is provided in the supporting information. The kinetics of electrocatalytic reactions is dependent on the electron and mass transfers, which are indicated by the Tafel slope. Smaller slopes indicate faster reactions. Among the materials studied here, Sr₃TiCoO_{7-δ} shows the smallest Tafel slope (Figure 4b), consistent with its higher HER electrocatalytic activity. The trend in kinetics is similar to that of the HER overpotential, where Sr₃TiFeO_{7-δ} and Sr₃TiMnO₇ have the next lowest Tafel slopes, followed by Sr₃Ti₂O₇.

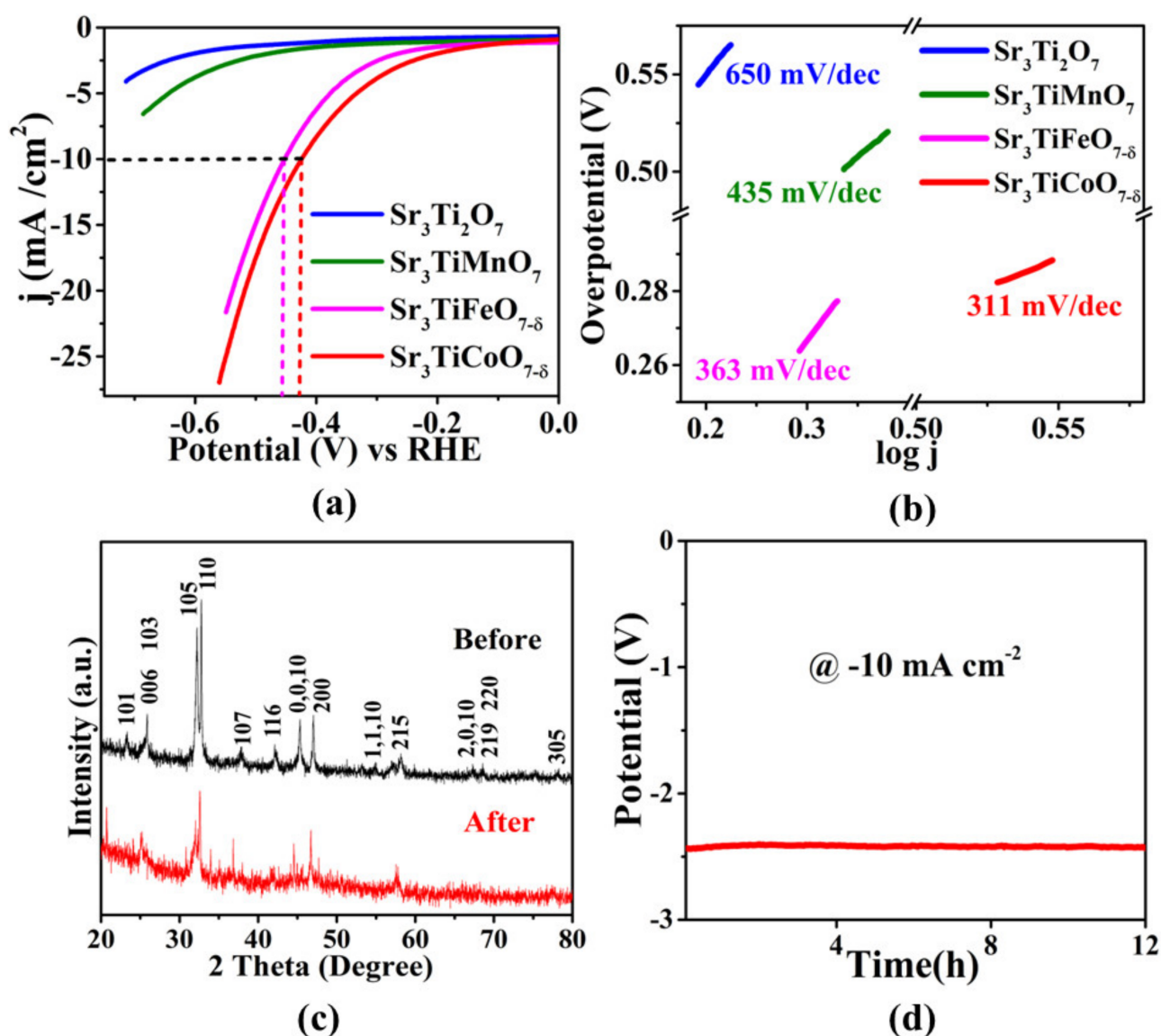


Figure 4. HER activity in 0.1 M KOH (a) polarization curves; (b) Tafel plots; (c) X-ray diffraction data of $\text{Sr}_3\text{TiCoO}_{7-\delta}$, before and after 100 cycles of OER; (d) chronopotentiometry response of $\text{Sr}_3\text{TiCoO}_{7-\delta}$ using a two-electrode cell consisting of nickel foam electrodes.

The electrocatalytic OER activities of the materials were also assessed. As evident from the polarization curves in Figure 5a, the electrocatalytic activities for OER show the same trend as HER, where $\text{Sr}_3\text{TiCoO}_{7-\delta}$ shows the lowest overpotential, $\eta_{10} = 456 \text{ mV}$ at $10 \text{ mA}/\text{cm}^2$, followed by $\text{Sr}_3\text{TiFeO}_{7-\delta}$, $\text{Sr}_3\text{TiMnO}_7$, and $\text{Sr}_3\text{Ti}_2\text{O}_7$. The difference in activity between the four materials is significant, where the OER responses obtained from the latter three materials do not even reach $10 \text{ mA}/\text{cm}^2$. However, the systematic change in current density is evident from Figure 5a. The overpotential (η_{10}) value obtained for $\text{Sr}_3\text{TiCoO}_{7-\delta}$ is lower than those of several oxides that have been reported before, such as $\text{La}_{0.5}\text{Sr}_{0.5}\text{Co}_{0.8}\text{Fe}_{0.2}\text{O}_3$ ($\eta_{10} = 600 \text{ mV}$) [33] and $\text{La}_{0.6}\text{Sr}_{0.4}\text{CoO}_{3-\delta}$ ($\eta_{10} = 590 \text{ mV}$) [34], but higher than those of some other oxides, such as $\text{CaSrFeMnO}_{6-\delta}$ ($\eta_{10} \approx 370 \text{ mV}$) [29] and $\text{LaCa}_2\text{Fe}_3\text{O}_8$ ($\eta_{10} = 360 \text{ mV}$) [31]. The OER kinetics was also studied, where the smallest Tafel slope (Figure 5b) was obtained for $\text{Sr}_3\text{TiCoO}_{7-\delta}$, indicating the fastest kinetics among the series, and consistent with its better OER activity. Chronopotentiometry experiments (Figure 5c) for $\text{Sr}_3\text{TiCoO}_{7-\delta}$ indicate a consistent response for at least 12 h. This is consistent with X-ray diffraction results after the OER, which show the retention of the structural integrity of the material (Figure 5d).

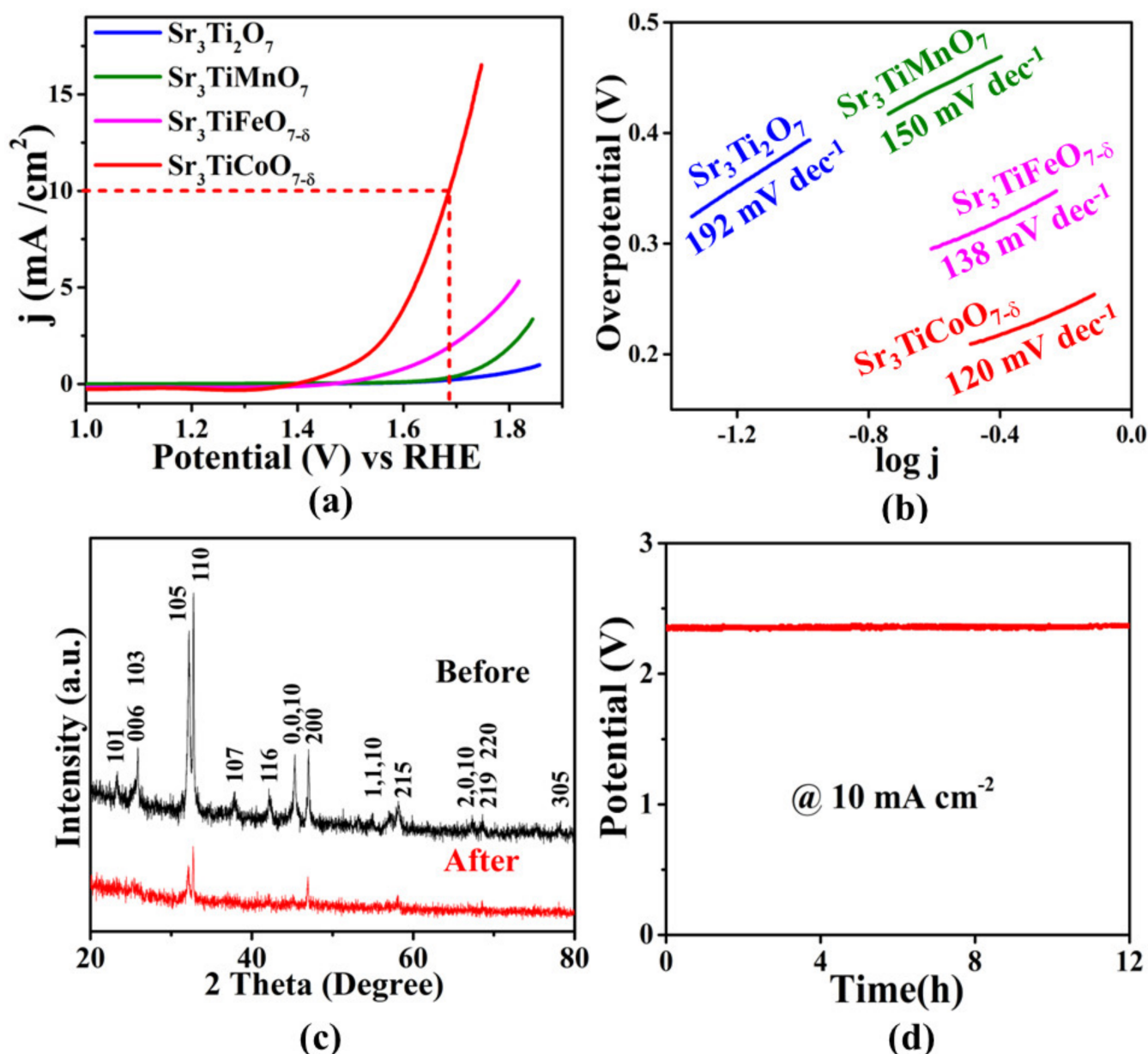


Figure 5. OER activity in 0.1 M KOH (a) polarization curves; (b) Tafel plots; (c) X-ray diffraction data of $\text{Sr}_3\text{TiCoO}_{7-\delta}$, before and after 100 cycles of OER; (d) chronopotentiometry response of $\text{Sr}_3\text{TiCoO}_{7-\delta}$ using a two-electrode cell consisting of nickel foam electrodes.

We also obtained the double-layer capacitance (C_{dl}) based on the equation $C_{dl} = j_{avg}/\nu$, using cyclic voltammograms acquired in the non-Faradaic region. Here, j_{avg} is the average of the absolute values of j_{anodic} and $j_{cathodic}$ at middle potential of the CV, and ν is the scan rate [35,36]. In the non-faradaic region, the current is primarily from the electrical double-layer charge and discharge where the electrode reactions are insignificant. The importance of C_{dl} is that it is proportional to the electrochemically active surface area [4,37]. The cyclic voltammograms obtained for the four compounds in the non-Faradaic region are shown in Figure 6a–d. Moreover, the plot of j_{avg} versus ν is depicted in Figure 6e, where the slope indicates the C_{dl} value. Among the four materials, $\text{Sr}_3\text{TiCoO}_{7-\delta}$ shows the largest C_{dl} , followed by $\text{Sr}_3\text{TiFeO}_{7-\delta}$, $\text{Sr}_3\text{TiMnO}_7$, and $\text{Sr}_3\text{Ti}_2\text{O}_7$. This is the same trend observed for the electrocatalytic activity for HER and OER, as well as the reaction kinetics.

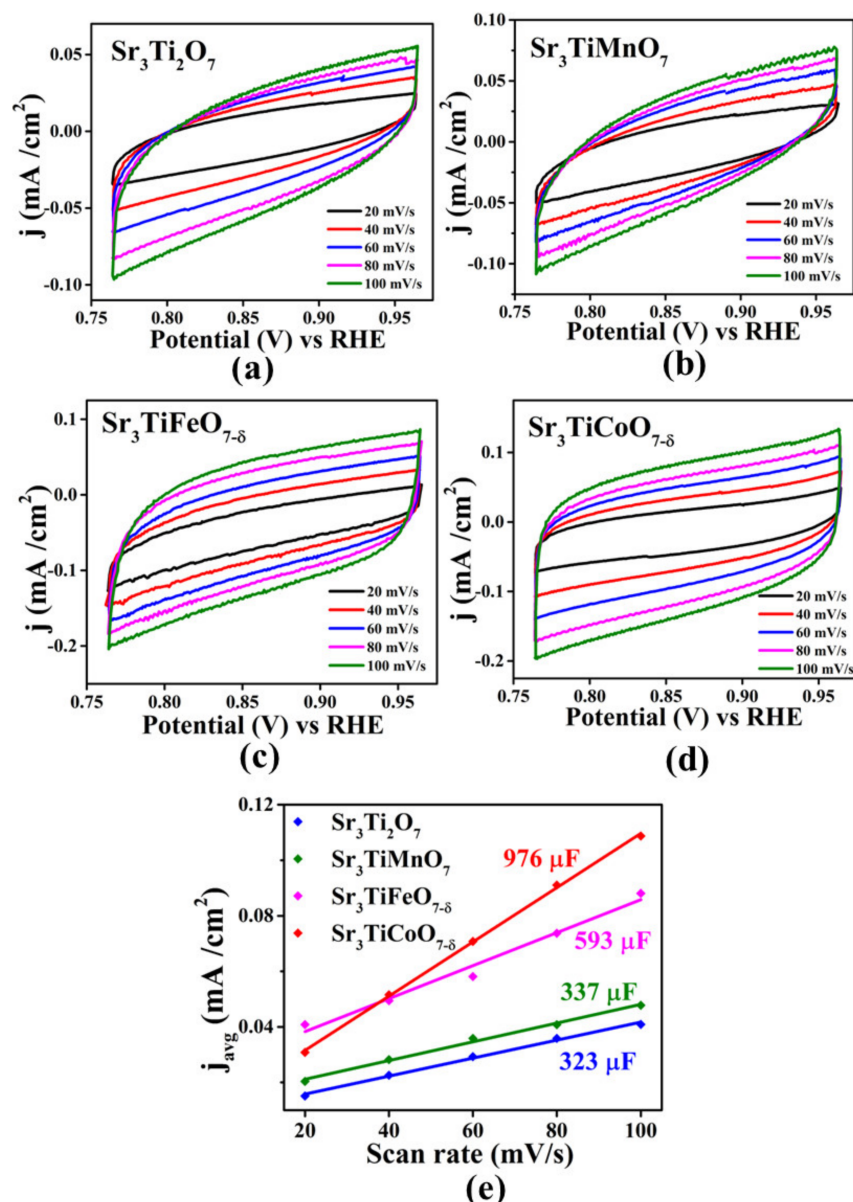


Figure 6. (a–d) cyclic voltammetry in non-Faradaic region in 0.1 M KOH; (e) j_{average} obtained from these CV plotted as a function of scan rate.

The active sites for oxide catalysts are often the metal sites [4,10,38]. Given that OER and HER mechanisms both involve electron transfer processes, the ability of the metal to change oxidation state during the electrochemical process will affect the catalytic activity [38,39]. This may be one of the reasons for better catalytic activities of $\text{Sr}_3\text{TiMnO}_7$, $\text{Sr}_3\text{TiFeO}_{7-\delta}$, and $\text{Sr}_3\text{TiCoO}_{7-\delta}$ compared to $\text{Sr}_3\text{Ti}_2\text{O}_7$. The two compounds, $\text{Sr}_3\text{TiCoO}_{7-\delta}$ and $\text{Sr}_3\text{TiFeO}_{7-\delta}$, which have better catalytic activities than the rest of the series, were found to contain oxygen vacancies by iodometric titrations, with $\text{Sr}_3\text{TiCoO}_{7-\delta}$ showing the highest concentration of oxygen vacancies ($\delta = 0.38$). Some previous studies on perovskite oxide electrocatalysts have indicated that oxygen vacancies can enhance the OER by increasing the adsorption energy of the reaction intermediates [40]. In some cases, oxygen vacancies may also lead to structural changes, which can enhance the electrocatalytic properties [35].

However, a number of other parameters may also have an impact on the electrocatalytic activity [39,41–44]. The electronegativity of the B-site is one of the descriptors studied before [45,46]. The higher electronegativity of Co relative to Fe, Mn, and Ti results in a decrease in the energy of the metal-to-ligand charge transfer [45,46], and an increase in bond covalency between the metal and oxygen [43], which can contribute to the improved

electrocatalytic properties of $\text{Sr}_3\text{TiCoO}_{7-\delta}$ compared to the other materials in this series. Some other descriptors studied before are the number of 3d electrons [41] and the e_g orbital occupancy [42]. Some studies have suggested that the e_g orbital occupancy of 1 is optimum for enhancing the electrocatalytic properties [4,10,44]. The presence of oxygen-vacancies in $\text{Sr}_3\text{TiCoO}_{7-\delta}$ and $\text{Sr}_3\text{TiFeO}_{7-\delta}$ indicates partial reduction of the transition metals into the trivalent state. While Fe^{3+} in oxides is often in a high-spin state ($t_{2g}^3 e_g^2$) [47], an intermediate spin state has been suggested for Co^{3+} ($t_{2g}^5 e_g^1$) [44,48], which contains one electron in e_g orbitals. Finally, a correlation between the electrical conductivity and electrocatalytic activity has been suggested before [9,49]. For the materials studied in this work, the trend in electrical conductivity matches that of the electrocatalytic performance, where $\text{Sr}_3\text{TiCoO}_{7-\delta}$ has the highest electrical charge transport and best catalytic activity.

3. Materials and Methods

3.1. Synthesis

Syntheses were performed using the solid-state method. Powders of SrCO_3 , TiO_2 , Mn_2O_3 , Fe_2O_3 , and Co_3O_4 were used to synthesize $\text{Sr}_3\text{Ti}_2\text{O}_7$, $\text{Sr}_3\text{TiMnO}_7$, $\text{Sr}_3\text{TiFeO}_{7-\delta}$, and $\text{Sr}_3\text{TiCoO}_{7-\delta}$. Stoichiometric amounts of oxides/carbonates were weighed and mixed thoroughly using agate mortar and pestle. The powder mixtures for $\text{Sr}_3\text{Ti}_2\text{O}_7$, $\text{Sr}_3\text{TiMnO}_7$, and $\text{Sr}_3\text{TiCoO}_{7-\delta}$ were initially pelletized and calcinated in air at 1250 °C for 24 h. Pure products of $\text{Sr}_3\text{Ti}_2\text{O}_7$ and $\text{Sr}_3\text{TiCoO}_{7-\delta}$ could be obtained after one additional grinding, palletization, and heating at the same temperature, 1250 °C, for 24 h. On the other hand, for $\text{Sr}_3\text{TiMnO}_7$, after the initial heating at 1250 °C, three additional re-palletization and re-heating were required, at 1250 °C for 24 h each, to obtain a pure product. For $\text{Sr}_3\text{TiFeO}_{7-\delta}$, a lower temperature (1180 °C) was needed to obtain a pure product. Synthesis efforts at 1250 °C led to an impure product. However, heating at 1180 °C for 10 h in air, followed by grinding, re-palletization, and re-heating under the same conditions, 1180 °C for 10 h in air, resulted in a pure product of $\text{Sr}_3\text{TiFeO}_{7-\delta}$. The heating and cooling rates of furnaces for all samples were 100 °C/hour.

3.2. Characterization

The synthesized polycrystalline oxides were studied using a high-resolution Cu $K\alpha_1$ X-ray diffractometer ($\lambda = 1.54056 \text{ \AA}$). Rietveld refinements for the X-ray diffraction data were carried out using GSAS software [50] and EXPGUI interface [51]. The electrical conductivity measurements were conducted using the two-probe technique on circular pellets, with an applied potential of 0.01 V in the temperature range of 25 to 800 °C. Iodometric titrations were performed to examine the oxygen contents of the materials [35]. Excess KI (2 g) and 50 mg of the sample were dissolved into 100 mL of argon-purged 1 M HCl, and the mixture was left overnight to react. Then, 5 mL of the reacted mixture (where iodine had been generated) was pipetted out and titrated against 0.025 M $\text{Na}_2\text{S}_2\text{O}_3$. A volume of 0.6 mL of a starch solution was used as an indicator near the endpoint of the titration. All steps of titration were conducted under argon. The excess KI causes the reduction of metal cations into ions that have the lowest stable oxidation state. Based on the concentration and titration volume of $\text{Na}_2\text{S}_2\text{O}_3$, the number of moles of titrant ($\text{Na}_2\text{S}_2\text{O}_3$) required to titrate 5 mL of the titrand is calculated. The quantity of I_2 that is titrated by $\text{Na}_2\text{S}_2\text{O}_3$ is directly related to the amount of oxygen lost as a result of the metals being reduced. The amount of oxygen in total is therefore equal to the sum of the oxygen that is still available (to maintain the charge balance with the reduced cations) and the oxygen that is lost (as a result of the reduction of metal ions).

3.3. Electrochemical OER/HER Measurements

The catalyst ink of each material was prepared by mixing 35 mg of the powder sample, 7 mg of carbon black powder, 40 μL Nafion[®] D-521 solution (5% w/w in water and 1-propanol) with 7 mL of THF (99%). The mixture was then sonicated for 30 min. Glassy carbon electrode (GCE, 5 mm diameter, 0.196 cm^2 area) was used as the working electrode

and was thoroughly cleaned prior to use. In the cleaning process, the GCE was refurbished using an aluminum oxide polishing suspension on a polishing cloth and sonicated for 2–3 min in ethanol. At the end of the cleaning steps, GCE was washed with deionized water before use. After sonication, the prepared catalyst ink was drop-casted on the glassy carbon electrode by placing two 10 μL coats (total of 20 μL) with a 2-min interval between the coats. Total catalyst mass loading on the GCE was 0.1 mg. Subsequently, the loaded GCEs were air-dried overnight before the OER/HER electrochemical measurements. Both acidic and basic electrolytes were tested. The electrochemical OER/HER measurements were performed in a standard three-electrode cell using a rotating disk electrode at 1600 rpm. A platinum electrode and a carbon electrode were used as counter electrodes in the OER and HER measurements, respectively. A commercial Hg/HgO electrode (1 M NaOH) was used for the OER/HER measurements in the basic medium as the reference electrode. The potential versus mercury/mercury oxide ($E_{\text{Hg}/\text{HgO}}$) was converted to be expressed against RHE using the equation $E_{\text{RHE}} = E_{\text{Hg}/\text{HgO}} + 0.059 \text{ pH} + E^0_{\text{Hg}/\text{HgO}}$, where $E^0_{\text{Hg}/\text{HgO}} = 0.097$ for 1 M NaOH [52]. A commercial Ag/AgCl electrode (4 M KCl) was used as the reference electrode for OER/HER experiments in the acidic medium. The equation $E_{\text{RHE}} = E_{\text{Ag}/\text{AgCl}} + 0.059 \text{ pH} + E^0_{\text{Ag}/\text{AgCl}}$ was used to convert the potential vs. silver/silver chloride ($E_{\text{Ag}/\text{AgCl}}$) to be represented against RHE where $E^0_{\text{Ag}/\text{AgCl}} = 0.197$ V for 4 M KCl [53,54]. Chronopotentiometry tests were conducted using two-electrode cells, with applied current of 10 mA. Each electrode was comprised 1 cm^2 of nickel foam, on which 100 μL of the catalyst ink had been drop-casted in 20 μL increments, followed by overnight air-drying. The two electrodes, which had been separated by two layers of glass fiber filter paper, were connected to gold leads and gold wires. The two electrodes were soaked in the electrolyte solution for least 12 h before performing the chronopotentiometry experiments.

Further experimental details, descriptions of analyses, and comparisons to the literature [55–69] is provided in the Supporting Information.

4. Conclusions

The trends in electrocatalytic activities of the Ruddlesden-Popper oxides studied in this work indicate the impact of several parameters on catalytic properties. The most active material in the series, $\text{Sr}_3\text{TiCoO}_{7-\delta}$, which shows the best catalytic performance for both HER and OER, also exhibits the highest electrical conductivity. In addition, it has the largest concentration of oxygen vacancies in the series. The oxygen vacancies lead to the reduction of metal ions, creating cations that have an optimum e_g electron occupancy for electrocatalytic activity. Furthermore, the higher electronegativity of cobalt, compared to Fe, Mn, and Ti, leads to enhanced bond covalency between the metal and oxygen, which can enhance the electrocatalytic properties.

Supplementary Materials: The following supporting information can be downloaded at: <https://www.mdpi.com/article/10.3390/inorganics11040172/s1>, Figure S1: Scanning electron microscopy images; Figure S2: EDX mapping analyses of (a) $\text{Sr}_3\text{TiCoO}_{7-\delta}$, (b) $\text{Sr}_3\text{TiFeO}_{7-\delta}$, (c) $\text{Sr}_3\text{TiMnO}_7$, and (d) $\text{Sr}_3\text{Ti}_2\text{O}_7$; Figure S3: X-ray photoelectron spectroscopy data showing the Ti spectra for all compounds (a), Mn for $\text{Sr}_3\text{TiMnO}_7$ (b), Fe for $\text{Sr}_3\text{TiFeO}_{7-\delta}$ (c), and Co for $\text{Sr}_3\text{TiCoO}_{7-\delta}$ (d). Figure S4: Impedance spectroscopy data to evaluate charge transfer resistance under (a) OER conditions, and (b) HER conditions. These data indicate that the trend in resistance is consistent with the trend in electrocatalytic activity, where the most active material has the smallest resistance; Figure S5: Polarization curves for OER in 0.1 M KOH with C_{dl} normalized current densities; Figure S6: X-ray diffraction data for (a) $\text{Sr}_3\text{Ti}_2\text{O}_7$, (b) $\text{Sr}_3\text{TiFeO}_{7-\delta}$, and (c) $\text{Sr}_3\text{TiMnO}_7$, before and after 100 cycles of OER in the 0.1 M KOH; Figure S7: X-ray diffraction data for (a) $\text{Sr}_3\text{Ti}_2\text{O}_7$, (b) $\text{Sr}_3\text{TiFeO}_{7-\delta}$, and (c) $\text{Sr}_3\text{TiMnO}_7$, before and after 100 cycles of HER in the 0.1 M KOH; Figure S8: The electronegativity increases from Mn to Fe and Co. The concentration of oxygen-vacancies increases from $\text{Sr}_3\text{TiMnO}_7$ to $\text{Sr}_3\text{TiFeO}_{7-\delta}$ and $\text{Sr}_3\text{TiCoO}_{7-\delta}$. The overpotential decreases from $\text{Sr}_3\text{TiMnO}_7$ to $\text{Sr}_3\text{TiFeO}_{7-\delta}$ and $\text{Sr}_3\text{TiCoO}_{7-\delta}$; Table S1: OER and HER overpotentials at 10 mA cm^{-2} (η_{10}) for some Sr-based oxides; A description of Tafel equation.

Author Contributions: Conceptualization, F.R.; methodology, C.C.W.K.-G. and F.R.; validation, C.C.W.K.-G.; formal analysis, C.C.W.K.-G.; investigation, C.C.W.K.-G.; resources, F.R.; data curation, C.C.W.K.-G. and F.R.; writing—original draft preparation, C.C.W.K.-G.; writing—review and editing, F.R.; visualization, C.C.W.K.-G.; supervision, F.R.; project administration, F.R.; funding acquisition, F.R. All authors have read and agreed to the published version of the manuscript.

Funding: This work is supported by the National Science Foundation (NSF) under grant no. DMR-1943085.

Data Availability Statement: The data presented in this study are available on request from the corresponding author.

Conflicts of Interest: The authors declare no conflict of interests.

References

1. Karki, S.B.; Ramezanipour, F. Magnetic and electrical properties of BaSrMMoO₆ (M = Mn, Fe, Co, and Ni). *Mater. Today Chem.* **2019**, *13*, 25–33. [[CrossRef](#)]
2. Fanah, S.J.; Ramezanipour, F. Lithium-ion mobility in layered oxides Li₂Ca_{1.5}Nb₃O₁₀, Li₂Ca_{1.5}TaNb₂O₁₀ and Li₂Ca_{1.5}Ta₂NbO₁₀, enhanced by supercell formation. *J. Energy Chem.* **2021**, *60*, 75–84. [[CrossRef](#)]
3. Fanah, S.J.; Yu, M.; Huq, A.; Ramezanipour, F. Insight into lithium-ion mobility in Li₂La(TaTi)O₇. *J. Mater. Chem. A* **2018**, *6*, 22152–22160. [[CrossRef](#)]
4. Alom, M.S.; Ramezanipour, F. Layered Oxides SrLaFe_{1-x}Co_xO_{4-δ} (x = 0 – 1) as Bifunctional Electrocatalysts for Water-Splitting. *ChemCatChem* **2021**, *13*, 3510–3516. [[CrossRef](#)]
5. Fanah, S.J.; Yu, M.; Ramezanipour, F. Experimental and theoretical investigation of lithium-ion conductivity in Li₂LaNbTiO₇. *Dalton Trans.* **2019**, *48*, 17281–17290. [[CrossRef](#)] [[PubMed](#)]
6. Fanah, S.J.; Ramezanipour, F. Strategies for Enhancing Lithium-Ion Conductivity of Triple-Layered Ruddlesden–Popper Oxides: Case Study of Li_{2-x}La_{2-y}Ti_{3-z}Nb_zO₁₀. *Inorg. Chem.* **2020**, *59*, 9718–9727. [[CrossRef](#)] [[PubMed](#)]
7. Kananke-Gamage, C.C.W.; Ramezanipour, F. Variation of the electrocatalytic activity of isostructural oxides Sr₂LaFeMnO₇ and Sr₂LaCoMnO₇ for hydrogen and oxygen-evolution reactions. *Dalton Trans.* **2021**, *50*, 14196–14206. [[CrossRef](#)]
8. Hona, R.K.; Huq, A.; Ramezanipour, F. Charge transport properties of Ca₂FeGaO_{6-δ} and CaSrFeGaO_{6-δ}: The effect of defect-order. *Mater. Chem. Phys.* **2019**, *238*, 121924. [[CrossRef](#)]
9. Hona, R.K.; Ramezanipour, F. Structure-dependence of electrical conductivity and electrocatalytic properties of Sr₂Mn₂O₆ and CaSrMn₂O₆. *J. Chem. Sci.* **2019**, *131*, 109. [[CrossRef](#)]
10. Alom, M.S.; Kananke-Gamage, C.C.W.; Ramezanipour, F. Perovskite Oxides as Electrocatalysts for Hydrogen Evolution Reaction. *ACS Omega* **2022**, *7*, 7444–7451. [[CrossRef](#)]
11. Shafir, O.; Shopin, A.; Grinberg, I. Band-Gap Engineering of Mo- and W-Containing Perovskite Oxides Derived from Barium Titanate. *Phys. Rev. Appl.* **2020**, *13*, 034066. [[CrossRef](#)]
12. Wang, Z.; Tan, S.; Xiong, Y.; Wei, J. Effect of B sites on the catalytic activities for perovskite oxides La₆Sr₄Co_xFe_{1-x}O_{3-δ} as metal-air batteries catalysts. *Prog. Nat. Sci.* **2018**, *28*, 399–407. [[CrossRef](#)]
13. Xu, X.; Pan, Y.; Zhong, Y.; Ran, R.; Shao, Z. Ruddlesden–Popper perovskites in electrocatalysis. *Mater. Horiz.* **2020**, *7*, 2519–2565. [[CrossRef](#)]
14. Forslund, R.; Hardin, W.; Rong, X.; Abakumov, A.; Filimonov, D.; Alexander, C.; Mefford, J.; Iyer, H.; Kolpak, A.; Johnston, K.; et al. Exceptional electrocatalytic oxygen evolution via tunable charge transfer interactions in La_{0.5}Sr_{1.5}Ni_{1-x}Fe_xO_{4±δ} Ruddlesden–Popper oxides. *Nat. Commun.* **2018**, *9*, 3150. [[CrossRef](#)] [[PubMed](#)]
15. Yin, B.; Li, Y.; Sun, N.; Ji, X.; Huan, Y.; Dong, D.; Hu, X.; Wei, T. Activating ORR and OER in Ruddlesden–Popper based catalysts by enhancing interstitial oxygen and lattice oxygen redox reactions. *Electrochim. Acta* **2021**, *370*, 137747. [[CrossRef](#)]
16. Reshak, A.H. Thermoelectric properties of Sr_{n+1}Ti_nO_{3n+1} (n=1, 2, 3, ∞) Ruddlesden–Popper Homologous Series. *Renew. Energy* **2015**, *76*, 36–44. [[CrossRef](#)]
17. Ge, W.; Zhu, C.; An, H.; Li, Z.; Tang, G.; Hou, D. Sol–gel synthesis and dielectric properties of Ruddlesden–Popper phase Sr_{n+1}Ti_nO_{3n+1} (n = 1, 2, 3, ∞). *Ceram. Int.* **2014**, *40*, 1569–1574. [[CrossRef](#)]
18. Navas, C.; Tuller, H.L.; Loye, H.-C.Z. Electrical conductivity and nonstoichiometry in doped Sr₃Ti₂O₇. *J. Eur. Ceram. Soc.* **1999**, *19*, 737–740. [[CrossRef](#)]
19. Nuansaeng, S.; Yashima, M.; Matsuka, M.; Ishihara, T. Mixed Conductivity, Nonstoichiometric Oxygen, and Oxygen Permeation Properties in Co-Doped Sr₃Ti₂O_{7-δ}. *Chem. Eur. J.* **2011**, *17*, 11324–11331. [[CrossRef](#)]
20. Sirikanda, N.; Matsumoto, H.; Ishihara, T. Effect of Co doping on oxygen permeation in Sr₃Ti₂O₇ with Ruddlesden–Popper structure. *Solid State Ion.* **2011**, *192*, 599–601. [[CrossRef](#)]
21. Chowki, S.; Sahu, B.; Singh, A.K.; Mohapatra, N. Dielectric response of double layered perovskite Sr₃MnTiO₇. *AIP Conf Proc* **2016**, *1731*, 090040.
22. Sharma, I.B.; Singh, C.; Singh, D. Synthesis, structure, electric transport and magnetic properties of Sr₃MnTiO_{7-δ}. *J. Alloys Compd.* **2004**, *375*, 11–14. [[CrossRef](#)]

23. Chowki, S.; Rayaprol, S.; Mukhopadhyay, A.; Mohapatra, N. Coexistence of spin glass type freezing and cooperative paramagnetic state in $\text{Sr}_3\text{MnTiO}_7$. *Phys. Rev. B* **2015**, *92*, 214416. [[CrossRef](#)]
24. Ruddlesden, S.N.; Popper, P. The compound $\text{Sr}_3\text{Ti}_2\text{O}_7$ and its structure. *Acta Crystallogr.* **1958**, *11*, 54–55. [[CrossRef](#)]
25. Zvereva, I.; Pavlova, T.A.; Pantchuk, V.; Semenov, V.; Breard, Y.; Choynet, J. The solid solution $\text{Sr}_3\text{Ti}_{2-x}\text{Fe}_x\text{O}_{7-\delta}$ ($x = 0.5$): Characterization of Fe (III)–Fe (IV) mixed valences. *Chim. Technol. Acta* **2016**, *3*, 46–57. [[CrossRef](#)]
26. Shannon, R.D. Revised effective ionic radii and systematic studies of interatomic distances in halides and chalcogenides. *Acta Crystallogr. Sect. A* **1976**, *32*, 751–767. [[CrossRef](#)]
27. Karki, S.B.; Ramezanipour, F. Pseudocapacitive Energy Storage and Electrocatalytic Hydrogen-Evolution Activity of Defect-Ordered Perovskites $\text{Sr}_x\text{Ca}_{3-x}\text{GaMn}_2\text{O}_8$ ($x = 0$ and 1). *ACS Appl. Energy Mater.* **2020**, *3*, 10983–10992. [[CrossRef](#)]
28. Hona, R.K.; Huq, A.; Mulmi, S.; Ramezanipour, F. Transformation of Structure, Electrical Conductivity, and Magnetism in $\text{AA}'\text{Fe}_2\text{O}_{6-\delta}$, $A = \text{Sr}, \text{Ca}$ and $A' = \text{Sr}$. *Inorg. Chem.* **2017**, *56*, 9716–9724. [[CrossRef](#)] [[PubMed](#)]
29. Hona, R.K.; Karki, S.B.; Ramezanipour, F. Oxide Electrocatalysts Based on Earth-Abundant Metals for Both Hydrogen- and Oxygen-Evolution Reactions. *ACS Sustain. Chem. Eng.* **2020**, *8*, 11549–11557. [[CrossRef](#)]
30. Hona, R.K.; Ramezanipour, F. Enhanced electrical properties in $\text{BaSrFe}_2\text{O}_{6-\delta}$ ($\delta = 0.5$): A disordered defect-perovskite. *Polyhedron* **2019**, *167*, 69–74. [[CrossRef](#)]
31. Karki, S.B.; Andriotis, A.N.; Menon, M.; Ramezanipour, F. Bifunctional Water-Splitting Electrocatalysis Achieved by Defect Order in $\text{LaA}_2\text{Fe}_3\text{O}_8$ ($A = \text{Ca}, \text{Sr}$). *ACS Appl. Energy Mater.* **2021**, *4*, 12063–12066. [[CrossRef](#)]
32. Feng, H.; Xu, Z.; Ren, L.; Liu, C.; Zhuang, J.; Hu, Z.; Xu, X.; Chen, J.; Wang, J.; Hao, W.; et al. Activating Titania for Efficient Electrocatalysis by Vacancy Engineering. *ACS Catal.* **2018**, *8*, 4288–4293. [[CrossRef](#)]
33. Park, H.W.; Lee, D.U.; Park, M.G.; Ahmed, R.; Seo, M.H.; Nazar, L.F.; Chen, Z. Perovskite-nitrogen-doped carbon nanotube composite as bifunctional catalysts for rechargeable lithium-air batteries. *ChemSusChem* **2015**, *8*, 1058–1065. [[CrossRef](#)]
34. Oh, M.Y.; Jeon, J.S.; Lee, J.J.; Kim, P.; Nahm, K.S. The bifunctional electrocatalytic activity of perovskite $\text{La}_{0.6}\text{Sr}_{0.4}\text{CoO}_{3-\delta}$ for oxygen reduction and evolution reactions. *RSC Adv.* **2015**, *5*, 19190–19198. [[CrossRef](#)]
35. Hona, R.K.; Ramezanipour, F. Effect of the Oxygen Vacancies and Structural Order on the Oxygen Evolution Activity: A Case Study of $\text{SrMnO}_{3-\delta}$ Featuring Four Different Structure Types. *Inorg. Chem.* **2020**, *59*, 4685–4692. [[CrossRef](#)] [[PubMed](#)]
36. Hona, R.K.; Karki, S.B.; Cao, T.; Mishra, R.; Sterbinsky, G.E.; Ramezanipour, F. Sustainable Oxide Electrocatalyst for Hydrogen- and Oxygen-Evolution Reactions. *ACS Catal.* **2021**, *11*, 14605–14614. [[CrossRef](#)]
37. Hona, R.K.; Ramezanipour, F. Remarkable Oxygen-Evolution Activity of a Perovskite Oxide from the $\text{Ca}_{2-x}\text{Sr}_x\text{Fe}_2\text{O}_{6-\delta}$ Series. *Angew. Chem.* **2019**, *131*, 2082–2085. [[CrossRef](#)]
38. Guan, D.; Zhou, J.; Huang, Y.-C.; Dong, C.-L.; Wang, J.-Q.; Zhou, W.; Shao, Z. Screening highly active perovskites for hydrogen-evolving reaction via unifying ionic electronegativity descriptor. *Nat. Commun.* **2019**, *10*, 3755. [[CrossRef](#)]
39. Bockris, J.O.M.; Otagawa, T. Mechanism of oxygen evolution on perovskites. *J. Phys. Chem.* **1983**, *87*, 2960–2971. [[CrossRef](#)]
40. Zhu, K.; Wu, T.; Li, M.; Lu, R.; Zhu, X.; Yang, W. Perovskites decorated with oxygen vacancies and Fe–Ni alloy nanoparticles as high-efficiency electrocatalysts for the oxygen evolution reaction. *J. Mater. Chem. A* **2017**, *5*, 19836–19845. [[CrossRef](#)]
41. Bockris, J.O.M.; Otagawa, T. The Electrocatalysis of Oxygen Evolution on Perovskites. *J. Electrochem. Soc.* **1984**, *131*, 290–302. [[CrossRef](#)]
42. Hong, W.T.; Risch, M.; Stoerzinger, K.A.; Grimaud, A.; Suntivich, J.; Shao-Horn, Y. Toward the rational design of non-precious transition metal oxides for oxygen electrocatalysis. *Energy Environ. Sci.* **2015**, *8*, 1404–1427. [[CrossRef](#)]
43. Suntivich, J.; Hong, W.T.; Lee, Y.-L.; Rondinelli, J.M.; Yang, W.; Goodenough, J.B.; Dabrowski, B.; Freeland, J.W.; Shao-Horn, Y. Estimating Hybridization of Transition Metal and Oxygen States in Perovskites from O K-edge X-ray Absorption Spectroscopy. *J. Phys. Chem. C* **2014**, *118*, 1856–1863. [[CrossRef](#)]
44. Suntivich, J.; May, K.J.; Gasteiger, H.A.; Goodenough, J.B.; Shao-Horn, Y. A Perovskite Oxide Optimized for Oxygen Evolution Catalysis from Molecular Orbital Principles. *Science* **2011**, *334*, 1383–1385. [[CrossRef](#)] [[PubMed](#)]
45. Saitoh, T.; Bocquet, A.E.; Mizokawa, T.; Fujimori, A. Systematic variation of the electronic structure of 3d transition-metal compounds. *Phys. Rev. B* **1995**, *52*, 7934–7938. [[CrossRef](#)] [[PubMed](#)]
46. Bocquet, A.E.; Mizokawa, T.; Saitoh, T.; Namatame, H.; Fujimori, A. Electronic structure of 3d-transition-metal compounds by analysis of the 2p core-level photoemission spectra. *Phys. Rev. B* **1992**, *46*, 3771–3784. [[CrossRef](#)] [[PubMed](#)]
47. Kan, W.H.; Chen, M.; Bae, J.-S.; Kim, B.-H.; Thangadurai, V. Determination of Fe oxidation states in the B-site ordered perovskite-type $\text{Ba}_2\text{Ca}_{0.67}\text{Fe}_{0.33}\text{NbO}_{6-\delta}$ at the surface (nano-scale) and bulk by variable temperature XPS and TGA and their impact on electrochemical catalysis. *J. Mater. Chem. A* **2014**, *2*, 8736–8741. [[CrossRef](#)]
48. Moritomo, Y.; Higashi, K.; Matsuda, K.; Nakamura, A. Spin-state transition in layered perovskite cobalt oxides: $\text{La}_{2-x}\text{Sr}_x\text{CoO}_4$ ($0.4 \leq x \leq 1.0$). *Phys. Rev. B* **1997**, *55*, R14725–R14728. [[CrossRef](#)]
49. Fan, L.; Rautama, E.L.; Lindén, J.; Sainio, J.; Jiang, H.; Sorsa, O.; Han, N.; Flox, C.; Zhao, Y.; Li, Y.; et al. Two orders of magnitude enhancement in oxygen evolution reactivity of $\text{La}_{0.7}\text{Sr}_{0.3}\text{Fe}_{1-x}\text{Ni}_x\text{O}_{3-\delta}$ by improving the electrical conductivity. *Nano Energy* **2022**, *93*, 106794. [[CrossRef](#)]
50. Larson, A.C.; Von Dreele, R.B. General Structure Analysis System (GSAS). In *Los Alamos National Laboratory Report LAUR*; NIST: Gaithersburg, MD, USA, 2004; pp. 86–748.
51. Toby, B.H. EXPGUI, a graphical user interface for GSAS. *J. Appl. Crystallogr.* **2001**, *34*, 210–213. [[CrossRef](#)]

52. Niu, S.; Li, S.; Du, Y.; Han, X.; Xu, P. How to Reliably Report the Overpotential of an Electrocatalyst. *ACS Energy Lett.* **2020**, *5*, 1083–1087. [[CrossRef](#)]
53. Du, X.; Ma, G.; Zhang, X. Experimental and Theoretical Understanding on Electrochemical Activation Processes of Nickel Selenide for Excellent Water-Splitting Performance: Comparing the Electrochemical Performances with M–NiSe (M = Co, Cu, and V). *ACS Sustain. Chem. Eng.* **2019**, *7*, 19257–19267. [[CrossRef](#)]
54. Du, X.; Su, H.; Zhang, X. Metal–Organic Framework-Derived Cu-Doped Co₉S₈ Nanorod Array with Less Low-Valence Co Sites as Highly Efficient Bifunctional Electrodes for Overall Water Splitting. *ACS Sustain. Chem. Eng.* **2019**, *7*, 16917–16926. [[CrossRef](#)]
55. Atuchin, V.V.; Gavrilova, T.A.; Grivel, J.C.; Kesler, V.G. Electronic structure of layered ferroelectric high-k titanate La₂Ti₂O₇. *J. Phys. D Appl. Phys.* **2009**, *42*, 035305. [[CrossRef](#)]
56. Liu, J.; Ma, X.; Yang, L.; Liu, X.; Han, A.; Lv, H.; Zhang, C.; Xu, S. In situ green oxidation synthesis of Ti³⁺ and N self-doped SrTiO_xN_y nanoparticles with enhanced photocatalytic activity under visible light. *RSC Adv.* **2018**, *8*, 7142–7151. [[CrossRef](#)]
57. Yang, H. The Structural and Morphology of (La_{0.6}Sr_{0.4})MnO₃ Thin Films Prepared by Pulsed Laser Deposition. *MATEC Web Conf.* **2016**, *44*, 02035. [[CrossRef](#)]
58. Zhu, J.; Guo, S.; Chu, Z.; Jin, W. CO₂-tolerant oxygen-permeable perovskite-type membranes with high permeability. *J. Mater. Chem. A* **2015**, *3*, 22564–22573. [[CrossRef](#)]
59. Lim, Y.-G.; Kim, D.; Lim, J.-M.; Kim, J.-S.; Yu, J.-S.; Kim, Y.-J.; Byun, D.; Cho, M.; Cho, K.; Park, M.-S. Anti-fluorite Li₆CoO₄ as an alternative lithium source for lithium ion capacitors: An experimental and first principles study. *J. Mater. Chem. A* **2015**, *3*, 12377–12385. [[CrossRef](#)]
60. Hona, R.K.; Huq, A.; Ramezanipour, F. Unraveling the Role of Structural Order in the Transformation of Electrical Conductivity in Ca₂FeCoO_{6-δ}, CaSrFeCoO_{6-δ}, and Sr₂FeCoO_{6-δ}. *Inorg. Chem.* **2017**, *56*, 14494–14505. [[CrossRef](#)]
61. Karmakar, A.; Kundu, S. A concise perspective on the effect of interpreting the double layer capacitance data over the intrinsic evaluation parameters in oxygen evolution reaction. *Mater. Today Energy* **2023**, *33*, 101259. [[CrossRef](#)]
62. He, B.; Tan, K.; Gong, Y.; Wang, R.; Wang, H.; Zhao, L. Coupling amorphous cobalt hydroxide nanoflakes on Sr₂Fe_{1.5}Mo_{0.5}O_{5+δ} perovskite nanofibers to induce bifunctionality for water splitting. *Nanoscale* **2020**, *12*, 9048–9057. [[CrossRef](#)] [[PubMed](#)]
63. Wu, X.; Yu, J.; Yang, G.; Liu, H.; Zhou, W.; Shao, Z. Perovskite oxide/carbon nanotube hybrid bifunctional electrocatalysts for overall water splitting. *Electrochim. Acta* **2018**, *286*, 47–54. [[CrossRef](#)]
64. Karki, S.B.; Hona, R.K.; Yu, M.; Ramezanipour, F. Enhancement of Electrocatalytic Activity as a Function of Structural Order in Perovskite Oxides. *ACS Catal.* **2022**, *12*, 10333–10337. [[CrossRef](#)]
65. Zhu, Y.; Zhou, W.; Zhong, Y.; Bu, Y.; Chen, X.; Zhong, Q.; Liu, M.; Shao, Z. A Perovskite Nanorod as Bifunctional Electrocatalyst for Overall Water Splitting. *Adv. Energy Mater.* **2017**, *7*, 1602122. [[CrossRef](#)]
66. Kananke-Gamage, C.C.W.; Ramezanipour, F. Effect of structural symmetry on magnetic, electrical and electrocatalytic properties of isoelectronic oxides A₂LaMn₂O₇ (A = Sr²⁺, Ca²⁺). *J. Phys. Chem. Solids* **2022**, *171*, 111013. [[CrossRef](#)]
67. Alom, M.S.; Ramezanipour, F. Electrocatalytic activity of layered oxides SrLaAl_{1/2}M_{1/2}O₄ (M = Mn, Fe, Co) for hydrogen- and oxygen-evolution reactions. *Mater. Chem. Phys.* **2023**, *293*, 126942. [[CrossRef](#)]
68. Anantharaj, S.; Noda, S. How properly are we interpreting the Tafel lines in energy conversion electrocatalysis? *Mater. Today Energy* **2022**, *29*, 101123. [[CrossRef](#)]
69. Shinagawa, T.; Garcia-Esparza, A.; Takanabe, K. Insight on Tafel slopes from a microkinetic analysis of aqueous electrocatalysis for energy conversion. *Sci. Rep.* **2015**, *5*, 13801. [[CrossRef](#)]

Disclaimer/Publisher’s Note: The statements, opinions and data contained in all publications are solely those of the individual author(s) and contributor(s) and not of MDPI and/or the editor(s). MDPI and/or the editor(s) disclaim responsibility for any injury to people or property resulting from any ideas, methods, instructions or products referred to in the content.